Growth of Secondary Dendrite Arms of Fe–C Alloy during Transient Directional Solidification by Phase-field Method

Yu XIE,[1)] Hongbiao DONG[1)]* and Jonathan DANTZIG[2,3)]

1) Department of Engineering, University of Leicester, Leicester LE1 7RH, UK.
2) Laboratory for the Simulation of Materials, EPFL, Lausanne 1015, Switzerland.
3) Department of Mechanical Science and Engineering, University of Illinois, Urbana, IL 61801, USA.

Due to the variations in the local solidification conditions in typical industrial casting processes, dendrites grow under transient rather than steady-state conditions. In this study, the phase-field method was used to study the evolution of secondary dendrite arms of Fe-0.3 wt.% C alloy during transient directional solidification imposed by decreasing the pulling velocity. We find that the dendrite under transient growth conditions is different from the steady-state dendrite, with smaller selection parameter σ^* and the dendrite envelope inside the parabola scaled by the tip radius. The secondary arms undergo a ripening process in which other secondary arms remelt by shrinking from their tips, rather than by detachment from the primary stalk. The surviving arms are finer than those found under steady-state growth conditions, and the size of the surviving arms decreases with decreasing growth velocity.

KEY WORDS: Fe–C alloy; solidification; dendritic growth; phase-field mothod.

1. Introduction

Dendrites are the predominant microstructural feature of cast metals, and the mechanical properties of the product depend strongly on the length scale and segregation pattern. Thus, understanding the shape and the length scale of a dendrite has been of interest in the casting field. Over the last few decades, a much better knowledge of steady free-growth dendrite has been obtained through the studies.

There are three regimes of a free-dendritic growth along the distance x_{tip} from the primary tip:

(1) The smooth tip regime free of secondary arms (or side branch) with $x_{tip} < 7$–$10 \, R_{tip}$ where R_{tip} is the tip radius. According to the solvability theory,[1,2] the anisotropy of the solid/liquid (S/L) interfacial energy has a significant effect on the shape of this regime. The steady-state R_{tip} is coupled to the steady-state tip velocity V_{tip} by the selection parameter $\sigma^* = \sqrt{d_0 D_l / (R_{tip}^2 V_{tip})}$ determined by the four-fold anisotropy coefficient.[3] Also, the shape of the tip regime is modified from the parabola (2D) or a paraboloid of revolution (3D) assumed in Ivantsov solution[4] to Ben Amar and Brener's needle crystal.[5] The form in 2D can be expressed as

$$\frac{|x_{tip}|}{R_{tip}} = \left(\frac{y / R_{tip}}{2} \right)^2 - A_4 \left(|y| / R_{tip} \right)^4 \quad \text{............ (1)}$$

where y is the distance from the central line of the dendrite.

(2) The initial secondary arm regime where the arms with small amplitude grow out on the primary stalk. This regime could be up to $x_{tip} < 30 \, R_{tip}$, and the connection of the arms tips forming an envelope whose form can be expressed as[6–10]

$$\frac{|x_{tip}|}{R_{tip}} = \alpha \left(|y| / R_{tip} \right)^{\beta} \quad \text{........................ (2)}$$

(3) The non-linear arming regime where the arms are under the complex ripening process during which the secondary arms of large size become coarser and otherwise remelt.[11] Although the evolution is complex, Beckerman et al.[9,10] found for the steady free-growth dendrite of SCN-acetone that the envelope of the arms can be still expressed in the form of Eq. (2) when x_{tip} is as large as $100 \, R_{tip}$.

Under directional solidification conditions, the solidified structure is not an isolated dendrite, but rather a dendritic array with another additional length scale, i.e. primary spacing λ_l. Experimental measurements[12] showed that λ_l is not a fixed value under a given thermal gradient G and pulling velocity V_p, but instead varies in a finite range, which also has been modelled numerically by Hunt et al.[13–15] However, the steady-state R_{tip} does not change with λ_l,[12,14–16] which thus implies that secondary arms largely contribute to the adjustment of the primary spacing. By contrast, direct observation of the secondary arm evolution under the steady constrained dendrite is rarely reported.

In practical casting processes, dendrites grow under transient growth conditions, i.e., where G and V_p evolve during growth.[17–22] The occurrence of arm detachment (fragmenta-

tion), which is one mechanism for columnar-to-equiaxed (CET) transition,[23,24] is reportedly more likely to happen under transient growth conditions. Lu *et al.* observed in SCN–H₂O that the ripening process under steady-state growth does not involve significant detachment of side branches except for a very long time (> 1 h).[16] However, over 30% of the secondary arms were detached within 20 mins when the pulling velocity was decreased after the steady state was achieved from an initially larger velocity.[25] These results indicate that evolution of the secondary arms during the transient growth condition is different from the steady-state behaviour. Therefore, in this study we aim to shed light on the secondary arm behaviour under transient growth conditions.

The phase-field (PF) method is commonly used to simulate dendritic growth because of its capability of tracking the S/L interface with high resolution at the micrometre scale.[26] Compared to the experimental techniques with comparable resolution to PF method, such as x-ray synchrotron radiation,[24] the PF method is of lower cost and easier data measurement. Several problems on dendritic growth, such as the orientation selection influenced by the anisotropy of S/L interfacial energy,[27–29] has been studied by the PF method.

In this work, we extended the PF code developed by Jeong *et al.*,[30,31] to include finite solid diffusivity[32] following the model proposed by Ohno and Matsuura.[33,34] It is thus applicable to industrial Fe–C alloys where the solid diffusivity of C solute is comparable to its liquid diffusivity.[35] In this study, the growth of secondary dendrite arms of Fe-0.3 wt.% C alloy during transient directional solidification imposed by decreasing the pulling velocity was investigated using the PF method. Comparisons were made between the steady-state and transient dendrites by quantitatively examining the dendrite envelope and by observing the coarsening and remelting of the secondary arms. In the following sections, we first describe the PF model, and then proceed to examine these results.

2. Phase-field Method

2.1. Phase-field Model

The PF method introduces a continuous variable ϕ that identifies the phases:[26] $\phi = +1$ in solid, $\phi = -1$ in liquid, and intermediate values correspond to the S/L interface. Thus, the S/L interface is treated as a diffuse field with a non-zero width (w). The thin-interface PF model for binary directional solidification originally proposed by Echebarria *et al.*[36] is used in the simulations. In this model, a dimensionless variable u is introduced to represent the concentration C, defined as

$$u = \ln \frac{C}{[(C_l^0 + C_s^0)/2 + h(\phi)(C_s^0 - C_l^0)/2]} \quad \text{........ (3)}$$

where $C_s^0 = k_e C_l^0$ and C_l^0 are the equilibrium solute concentrations in the solid and the liquid at temperature T_l^0, respectively. k_e is the equilibrium partition coefficient assumed to be constant, and $h(\phi)$ is the interpolation function defined as $h(\phi) = \phi$.

The evolution equation for ϕ and C for directional solidification are

$$\tau \frac{\partial \phi}{\partial t} = w^2 \nabla^2 \phi + (\phi - \phi^3)$$
$$- \frac{\lambda}{(1-k_e)}(1-\phi^2)^2 \left[e^u - 1 + \frac{(x - x_0 - V_p t)(1 - k_e)}{l_T} \right]$$
$$\text{........................ (4)}$$

$$\frac{\partial C}{\partial t} = \nabla \cdot \left[\tilde{q}(\phi) D_l e^u \frac{C_l^0 [1 + k_e - (1 - k_e) h(\phi)]}{2} \nabla u \right] - \nabla \cdot j_{at}$$
$$\text{........................ (5)}$$

where t is time. In Eq. (4), τ is the characteristic kinetic time constant and λ is a dimensionless parameter, both of which will be further discussed below. $(x–x_0–V_p t)(1–k_e)/l_T$ couples the phase field to the temperature field in directional solidification assuming the sample is pulled through the temperature gradient G at velocity V_p. In this expression, x is the coordinate and x_0 is the position at time $t = 0$ where the temperature is T_l^0, and $l_T = |m_e|(1–k_e)C_l^0/G$ with m_e the liquidus slope. To correctly describe the S/L interfacial energy and the Gibbs-Thomson equation at the S/L interface with the negligible interface attachment kinetics, the following relations are required

$$\lambda = \alpha_1 w / d_0; \quad \tau = \alpha_2 \frac{\lambda w^2}{D_l} \quad \text{.................... (6)}$$

where $\alpha_1 = 0.8839$ and $\alpha_2 = 0.6267$[36]

In Eq. (5), $\tilde{q}(\phi)D_l$ is the solute diffusivity for the entire solidification domain; $\tilde{q}(+1) = D_s/D_l$ in solid, $\tilde{q}(-1) = 1$ in liquid. j_{at} is the anti-trapping current introduced to reduce artificial solute trapping and is expressed as

$$j_{at} = -a(\phi)w(1 - k_e)C_l^0 e^u \frac{\partial \phi}{\partial t} \frac{\nabla \phi}{|\nabla \phi|} \quad \text{.............. (7)}$$

To include the solid diffusivity in the model, the expressions of $\tilde{q}(\phi)$ and $a(\phi)$ proposed by Ohno and Matsuura[33] are adopted, *i.e.*

$$\tilde{q}(\phi) = \frac{1 - \phi + k_e \frac{D_s}{D_l}(1 + \phi)}{1 + k_e - (1 - k_e)\phi}; \quad a(\phi) = \frac{1}{2\sqrt{2}}\left(1 - k_e \frac{D_s}{D_l}\right)$$
$$\text{........................ (8)}$$

The S/L interfacial energy γ_{sl} and its anisotropy (*i.e.* its dependence on the interface normal $\vec{n}$) can be expressed, for a crystal with cubic symmetry, in terms of cubic harmonics[37]

$$\gamma_{sl}(\vec{n}) = \gamma_{sl}^0 a_n;$$
$$a_n = 1 + a_1 \left(Q - \frac{3}{5}\right)a_1 + a_2 \left(3Q + 66S - \frac{17}{7}\right) + ... \quad \text{.... (9)}$$

where $\vec{n}$ is the normal vector to the surface in the reference frame, γ_{sl}^0 is the orientation-averaged interfacial energy, a_1 and a_2 are the first two anisotropy coefficients, and the cubic harmonics Q and S are defined in terms of the Cartesian components of $\vec{n}$ as

$$Q = \frac{n_x^4 + n_y^4 + n_z^4}{(n_x^2 + n_y^2 + n_z^2)^2}; \quad S = \frac{n_x^2 n_y^2 n_z^2}{n_x^2 + n_y^2 + n_z^2} \quad \text{........ (10)}$$

The anisotropy is incorporated into the PF model by defining $w = w_0 a_n$ and $\tau = \tau_0 a_n^2$.[3] Note that the anisotropy expression Eq. (9) admits several preferred dendrite growth orienta-

tions, including <100>, <110> and <111> in 3D.

The dynamics of sidebranch initiation has been attributed to selective amplification of noise,[38,39] and to deterministic oscillations near the dendrite tip.[40,41] In this work, we do not add noise to the equations. However, there remains some residual grid noise that contributes to the growth of sidebranches in our simulations. These sidebranches tend to start farther from the tip than they would if noise were to be included. Thus, our simulations do not address the question of differentiating between these two mechanisms. Nevertheless, our focus here is on the evolution by coarsening of arrays of sidebranches, which is not affected by their origin.

2.2. Parameter Selection

The nominal composition of the model Fe–C alloy is $C_0 =$ 0.3 wt.%, and the material properties used in the simulations are shown in **Table 1**. There is no accepted experimental value in the literature for the anisotropy in S/L interfacial energy for Fe–C alloys.[42] In our simulations, the input S/L interfacial energy and its anisotropy listed in Table 1 were obtained from the MD modelling provided by Liu $et\ al.$[43] We used $G = 150$ K/mm and $V_p = 8$/mm for the base case, corresponding to the conditions at one point of the weld pool obtained by the front-tracking modelling carried out by the MintWeld project partners at University College Dublin National University of Ireland, Ireland.[44] We used $w = 0.08$ μm, which was determined by numerical experimentation to give consistent converged results.

Two-dimensional (2D) simulations were performed in this study by using thin samples with $L_x = L_y \gg L_z$, as the transition from the 3D to 2D was observed due to the refinement in one direction.[31] Because of the cubic symmetry, only 1/4 cylinder seed of radius $r_0 = 4w$ and height $h = L_z$ was placed at the origin to initiate the solid. G and V_p were imposed along the x-axis, which was also parallel to the <001> axis of the crystal. The length of y-axis was $L_y = 1/2$ λ_l where λ_l was the primary spacing of the dendrite/cell array. Because the λ_l varies in a finite range under given directional solidification conditions,[13–15] we examined a variety of spacings. The secondary arms were suppressed when λ_l was less than 15.36 μm. In the results shown below, $\lambda_l = 40.96$ μm was selected, which allowed the outgrowth of secondary arms. Symmetry boundary conditions were imposed on the x-y face and x-axis was long enough that the solutal boundary layer ahead of the tip never approached the far boundary.

Steady state was reached at time $t = 0.009$ s for $V_p = 8$

Table 1. Material properties of the modelled Fe-0.3 wt.% C alloy.

| Materials Properties		
	Value	Source
Equilibrium partition coefficient	0.176	thermodynamic calculation
Liquidus slope (K/(wt.%))	−80	thermodynamic calculation
Liquid diffusivity (m^2/s)	2×10^{-8}	45)
Solid diffusivity (m^2/s)	5.57×10^{-9}	45)
Interfacial energy(J/m^2)	0.164	MD calculation
Anisotropy a_1	0.0288	MD calculation
Anisotropy a_2	−0.000612	MD calculation

mm/s, defined as when $V_{tip} = V_p$. The morphology at $t =$ 0.009 s is shown in **Fig. 1**. The sharp shape of the primary tip indicates that the obtained solidified structure under the concerned condition is dendritic rather than cellular. It can be seen that the secondary arms initially grew in different directions with different sizes that were determined during the later ripening process.

Transient growth conditions were then imposed by decreasing the pulling velocity from $V_p = 8$ mm/s to $V_p = V_f$ after the dendritic growth reached the steady state at $t =$ 0.009 s. We examined several values for V_f: 4 mm/s, 2 mm/s to 1 mm/s. **Figure 2** shows the evolution of V_{tip} vs. t for the various V_f, indicating that the dendrite begun to evolve under the transient condition due to the change in V_p. As shown in Fig. 2, V_{tip} gradually approached V_f, whereupon a new steady state was achieved for the new pulling velocity. Our concern is the transient stage and therefore we stopped the calculations at that point The evolution of the dendritic growth during the transient growth condition with an emphasis on the secondary arms will be discussed below.
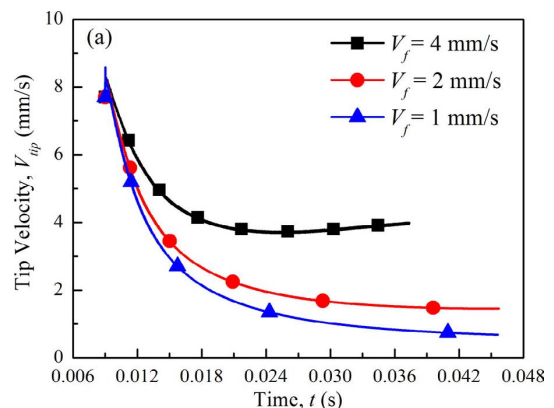
3. Results and Discussion

3.1. Tip Radius

The plots of R_{tip} vs. t under different conditions given in **Fig. 3** show that R_{tip} went into the steady state at time $t =$
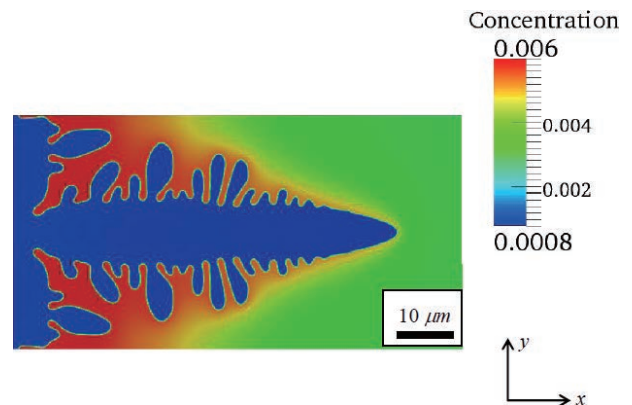
Fig. 1. The morphology at $t = 0.009$ s, when the dendritic growth had reached steady state at the initial higher velocity $V_p = 8$ mm/s.

Fig. 2. Evolution of tip velocity after the pulling velocity was decreased during the dendritic growth. (Online version in color.)
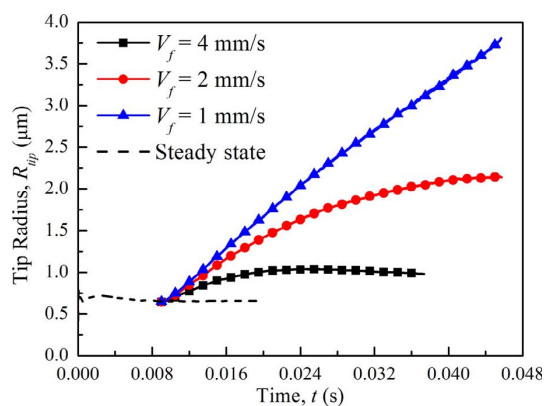
Fig. 3. Evolution of tip radius under various growth conditions. (Online version in color.)

Fig. 4. Evolution of selection parameter under various growth conditions. (Online version in color.)

Fig. 5. The dendrite envelopes at different times on the steady-state evolution with the primary tips located at the origin. (Online version in color.)

0.009 s for the initial $V_p = 8$ mm/s and kept as constant if it continued to grow under steady state where V_p was not changed afterwards (dash line). The steady-state R_{tip} obtained by the PF method is 0.66 μm, close to the value of 0.67 μm given by the KGT prediction.[46] The closeness of the agreement between the PF and KGT results is probably fortuitous. By contrast, when the V_p was decreased to a lower value $V_p = V_f$ after $t = 0.009$ s, as shown in Fig. 3, the R_{tip} began to increase corresponding to the decrease in the V_{tip} (Fig. 2). At the same solidification time, the R_{tip} is smaller at the higher V_f while V_{tip} is larger as can be seen in Fig. 2. The trends of R_{tip} varying with V_{tip} under the steady-state and transient growth conditions all qualitatively complied with that predicted by solvability theory.[1,2]

Quantitatively, the selection parameter σ^* was examined and plots of σ^* vs. t during transient growth conditions are shown in **Fig. 4**. The selection parameter obtained in steady-state growth did not persist under the transient growth condition. For each value of V, the selection parameter began to decrease after V_p was decreased, with a larger decrease for larger velocity changes. Thus, we find that the selection parameter is not constant when V_p changes.

3.2. Dendrite Envelope
3.2.1. Steady-state Evolution
With the primary stalk advancing during the dendritic growth, new secondary arms grow out with distance from the primary tip, and the arms away from the tip undergo a complex ripening process, where the secondary arms grow competitively with their neighbours. Some of the secondary arms survive and become coarser, whereas others remelt. The dendrite envelope is commonly used to characterize the complex morphology including the secondary arms.[5,8–10] This envelope consists of the smooth contour of the primary tip region and the connection of the 'active' (or surviving) arm tips.

The dendrite envelopes at different times on the steady-state evolution are plotted in **Fig. 5** for various times, with the primary tip always located at the origin. It can be seen that the contours of the tip regime before the secondary arms exactly overlap, meaning that the primary tip regime evolves in a shape-conserving manner. By contrast, secondary arm tips at different times were located at different positions. However, if the connection of those tips (dendrite envelope) rather than the separate tips, were examined, it
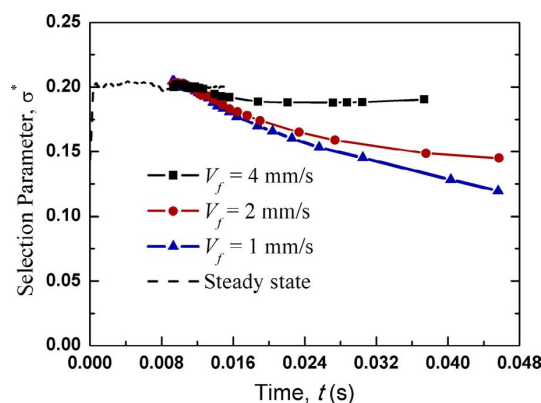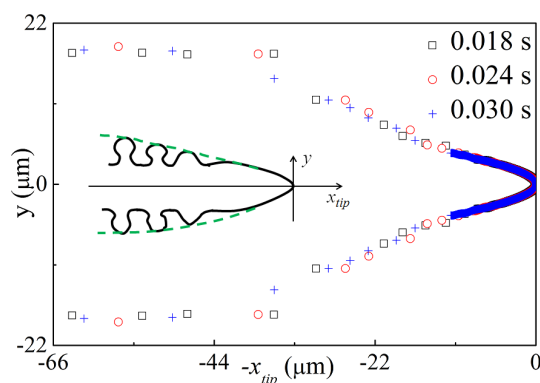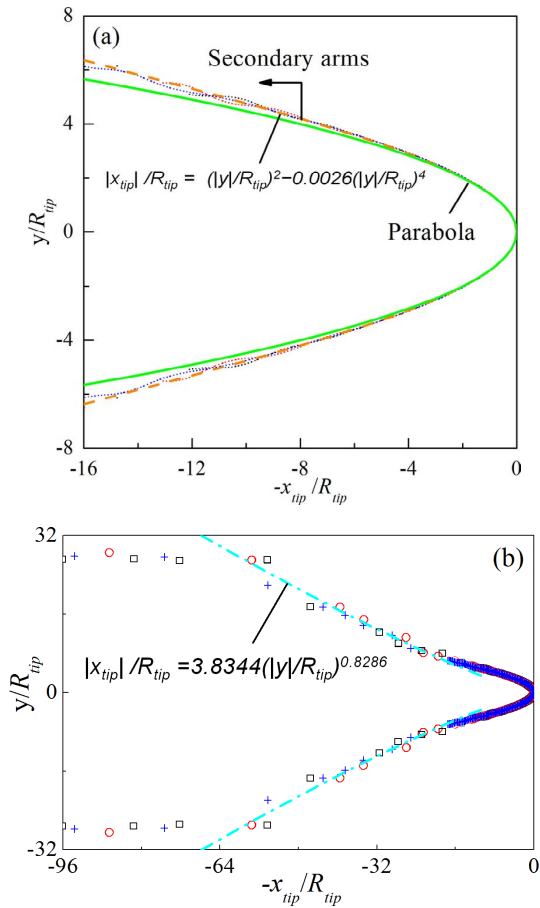
can be seen that the dendrite envelopes at different times overlap indicating that the dendrite envelope evolves in a shape-conserving manner, in agreement with the experimental observation on the secondary arm evolution of SCN-acetone under steady-state free growth.[9,10]

As mentioned in the Introduction, the geometric parameters of the dendrite can be scaled by the R_{tip}, and thus the dendrite envelopes in Fig. 5 were re-plotted with x_{tip} and y scaled by R_{tip} obtained by phase-field simulation. The result is shown in **Fig. 6**. Figure 6(a) is limited to the tip regime, which also includes a parabola expressed as $\dfrac{|x_{tip}|}{R_{tip}} = \left(\dfrac{|y|/R_{tip}}{2}\right)^2$. It can be seen that for $x_{tip}/R_{tip} < 4$ the tip regime fits well with the parabola. For a four-fold symmetric crystal, it has been predicted by Ben Amar and Brener that the inclusion of the capillary effect brings a deviation from a parabola with the form given by Eq. (1).[5] The least-squares fit of the data shown in Fig. 6(a) indicates that a good fit is still achieved when x_{tip}/R_{tip} is as large as $x_{tip}/R_{tip} = 10$ with $A_4 = 0.0026$, indicating that the steady-state tip regime is more close to the Ben Amar and Brener needle crystal, in agreement with the work of Karma et al.[8] The obtained value A_4 is much smaller than the value 1/96 predicted by solvability theory, but closer to the one (from 0.004 to 0.005) obtained by Karma et al. using phase-field model[8] and to the values (0.004 in pure SCN and 0.005 in SCN-acetone alloys) measured by Melendez and Beckermann.[9]

Fig. 6. The dendrite envelopes at different times on the steady-state evolution located in the coordinate system scaled by the tip radius. (Online version in color.)

Fig. 7. The dendrite envelope at time $t = 0.03$ s under the transient growth condition for $V_f = 1$ mm/s located in the coordinate system scaled by the tip radius. (Online version in color.)

For the regime outlined by the secondary arm tips, the least-squares fit from Eq. (2) shows that for $10 < x_{tip}/R_{tip} < 50$, the secondary tip positions can be correlated by
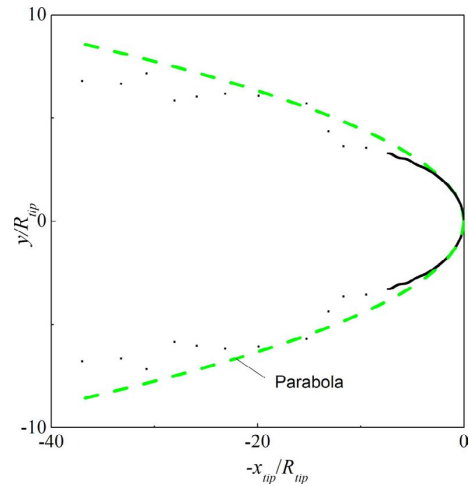
$$\frac{|x_{tip}|}{R_{tip}} = 3.8344 \left(|y| / R_{tip}\right)^{0.8286} \quad \text{................. (11)}$$

For a steady free dendrite, the reported power β is greater than 1[8–10] different from our fitted value, which means that the normalized amplitude of the arms is larger under free growth than that under the directional solidification. This may be attributed to the constrained spacing by the primary spacing for the arms growing. It can be also seen that when $z/R_{tip} > 50$, the contour of the dendrite envelope is almost parallel with the x-axis and the width is constrained by the primary spacing.

3.2.2. Transient Growth Conditions

As discussed above, the dendritic envelope at different times during steady-state evolution can be scaled by the steady-state R_{tip} using the reported expressions (Eqs. (1) and (2)) when $x_{tip}/R_{tip} < 50$. To compare the computed shapes at various times, the geometry at each time was scaled by the value of R_{tip} at that time, and each dendrite was translated such that its tip corresponded to $x_{tip}/R_{tip} = 0$.

Figure 7 is the dendrite envelope at time $t = 0.03$ s under the transient growth condition for $V_f = 1$ mm/s scaled by the value $R_{tip} = 2.5 \ \mu$m. The parabola was also plotted in the same figure for comparison. It can be seen that the contour

at the tip regime does not fit with the parabola again but instead is included by the parabola. Surprisingly, the regime of the dendrite envelope with the secondary arms growing out is also inside in the parabola, as shown in Fig. 7. It is different from the steady-state dendrite where the dendrite envelope is outside the parabola, indicating that the development of the dendrite envelope is retarded with the increasing tip radius under the transient growth condition. It may be because R_{tip} increased much faster than that predicted by the solvability theory as shown in Fig. 4.

3.3. Coarsening of the Secondary Arms

Figure 8 shows the evolution of the secondary close to the dendrite bottom at time $t = 0.012$ s and $t = 0.030$ s under steady-state growth conditions. As shown in Fig. 8(a), the secondary arms at earlier time are in different orientations as observed in the experiments,[9,10] indicating that the growth direction of the secondary arms after their outgrowth at a distant from the tip is not in the preferred orientation determined by the S/L interfacial anisotropy, which is different from the behaviour of the primary stalk.

However, through competitive growth, as shown in Fig. 8(b), the surviving secondary arms (marked by the numbers) become coarser with almost the same orientation, which should be the preferred orientation determined by the anisotropy in interfacial energy. Thus it indicates that the surviving secondary arms are those which grew in the preferred orientations and those relatively deviated from the preferred orientations remelted during the competitive growth. It can be seen that the preferred orientation is not vertical to the primary stalk but tilted towards <110> around 12 degrees. The tilting of the secondary arms can be attributed to the inclusion of the secondary anisotropy coefficient (a_2 in Eq. (9)) in the simulations, which gives additional preferred orientation <110>,[28] as well as the fact that the solute field is not parallel to the pulling direction. It can also be seen that the arms between those surviving arms in Fig. 8(a), which are smaller than their neighbours, disappeared after competitive growth. The detailed manner in which they remelted will be discussed further in Section 3.4.

Figure 9 shows the morphologies after competitive

growth of secondary arms under the transient growth condition for various V_f. The morphology obtained under the steady state shown in Fig. 8(b) was also plotted in Fig. 9 for comparison. Note that the morphologies shown in Fig. 9 were not at the same solidification time because the morphologies at the same solidification time under various conditions are not in the same ripening stage, and thus are not comparable. Therefore we compared the surviving secondary arms at the solidification times when the arms between those surviving arms had almost disappeared.

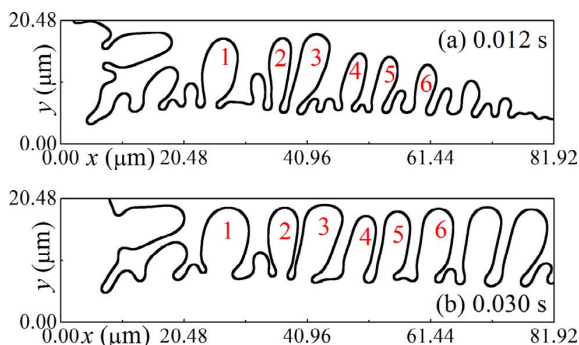Figure 9 shows that the surviving secondary arms under the transient growth conditions are those that survived under the steady-state growth condition. Thus whether under the steady-state growth condition or under the transient growth condition, the secondary arms with the preferred orientations survived and became coarser during the competitive growth. However, it can be found that the surviving arms were finer under transient growth conditions than under constant growth velocity, and the necklaces connecting the arms to the primary stalk were finer. Furthermore, the size of the surviving arms decreases with decreasing growth velocity as shown in Fig. 9, indicating that it is the decrease in the tip velocity that leads to the finer secondary arms.

3.4. Remelting of the Secondary Arms

The detachment of the secondary arms is related to the question on how the secondary arms remelted during the competitive growth; the detachment will happen if the remelting of the secondary arms occurs at the necklace through which the secondary arms are connected to the primary stalk. Therefore, we examined the remelting process of all the secondary arms that happened in the simulations under both steady-state and transient growth conditions. Only one manner of remelting is observed and the typical remelting process is shown in **Fig. 10** in which the secondary arms between the surviving arms gradually remelted with time.

Initially at time $t = 0.009$ s (Fig. 10(a)), several secondary arms existed between the surviving arm marked as 1 and 2. During the growth of the secondary arms, solute was rejected and accumulated in the grooves between the surviving arms, and thus it can be seen that the liquid concentration around the surviving arms was lower than that around the arms between them. The higher solute concentration means lower melting temperature, and the arms remelt once the local temperature is higher than the local melting temperature. Thus it can be seen from Fig. 10(b) that the smaller two arms have firstly entirely remelted at time $t = 0.015$ s. With time evolving, the other relatively larger arms between the arm 1 and 2 gradually remelted while the surviving arms 1

Fig. 8. Morphologies close to the dendrite bottom at time $t = 0.012$ s and $t = 0.030$ s under the steady-state growth condition. (Online version in color.)
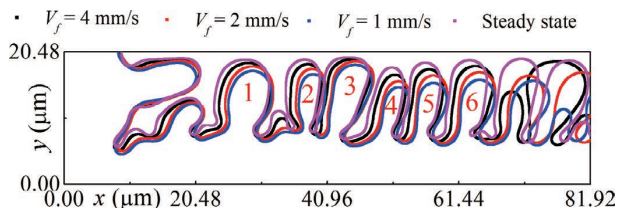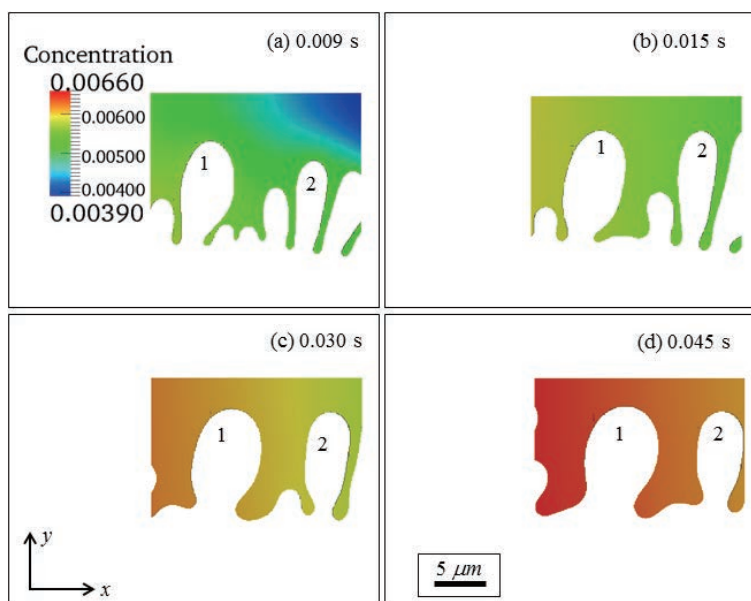

Fig. 9. Morphologies close to the dendrite bottom after the competitive growth of secondary arms under various growth conditions.

Fig. 10. Typical remelting process observed in the simulations. In this case, the dendritic grew under the transient growth condition with $V_f = 1$ mm/s.

and 2 became coarser as discussed earlier.

Importantly, Fig. 10 demonstrates that the remelting of the secondary arms started from the tip with decreased height while the necklace width became coarser. When it was totally remelted, the coarser necklace became part of the primary stalk. Thus, the secondary arms remelted by shrinking from the tip rather than by detachment from the primary stalk at the necklace.

As discussed above, the detachment of the secondary arms was not observed in our study. In the literature, besides the transient growth condition, the detachment was observed when the flow was also included.[47] Note that in the experiments carried out by Lu et al.,[25] the flow was an uncontrolled factor. Therefore, if the flow is a necessary factor in the occurrence of the detachment of the secondary arms under the transient growth condition needs further study.

4. Conclusions

In this study, the phase-field method was used to study the evolution of secondary dendrite arms of Fe-0.3 wt.% C alloy during transient directional solidification imposed by decreasing the pulling velocity. Dendrite envelope, the coarsening and remelting of the secondary arms under the transient growth condition were concerned. Under the transient growth condition with the tip velocity decreasing,

(1) The selection parameter $\sigma*$ is smaller than that under the steady-state condition.

(2) The dendrite envelope cannot be scaled by the tip radius and the part of the dendrite envelope with secondary arms is within the parabola, which is different from the steady-state dendrite envelope where the dendrite envelope can be fitted by the reported expressions within $x_{tip}/R_{tip} < 50$ and the part with secondary arms is within the parabola.

(3) The surviving secondary arms, which became coarser through the ripening process, are finer than those under steady-state growth condition. Furthermore, the size of the surviving arms decreases with decreasing growth velocity.

(4) The secondary arms remelted by shrinking from the tip. Detachment from the primary stalk at the necklace was not observed.

REFERENCES

1) D. A. Kessler, J. Koplik and H. Levine: *Adv. Phys.*, **37** (1988), 255.
2) A. Barbieri and J. S. Langer: *Phys. Rev. A*, **39** (1989), 5314.
3) A. Karma and W.-J. Rappel: *Phys. Rev. E*, **57** (1998), 4323.
4) G. P. Ivantsov: *Dokl. Akad. Nauk SSR*, **58** (1947), 567.
5) M. Ben Amar and E. Brener: *Phys. Rev. Lett.*, **71** (1993), 589.
6) R. Almgren, W.-S. Dai and V. Hakim: *Phys. Rev. Lett.*, **71** (1993), 3461.
7) E. Brener: *Phys. Rev. Lett.*, **71** (1993), 3653.
8) A. Karma, Y. H. Lee and M. Plapp: *Phys. Rev. E*, **61** (2000), 3996.
9) A. J. Melendez and C. Beckermann: *J. Cryst. Growth*, **340** (2012), 175.
10) Q. Li and C. Beckermann: *Phys. Rev. E*, **57** (1998), 3176.
11) R. Trivedi and K. Somboonsuk: *Mater. Sci. Eng.*, **65** (1984), 65.
12) H. Weidong, G. Xingguo and Z. Yaohe: *J. Cryst. Growth*, **134** (1993), 105.
13) M. H. Burden and J. D. Hunt: *J. Cryst. Growth*, **22** (1974), 109.
14) J. D. Hunt and S.-Z. Lu: *Metall. Mater. Trans. A*, **27** (1996), 611.
15) S.-Z. Lu and J. D. Hunt: *J. Cryst. Growth*, **123** (1992), 17.
16) G. Hansen, S. Liu, S.-Z. Lu and A. Hellawell: *J. Cryst. Growth*, **234** (2002), 731.
17) X. He, P. W. Fuerschbach and T. DebRoy: *J. Phys. D: Appl. Phys.*, **36** (2003), 1388.
18) W. Zhang, G. G. Roy, J. W. Elmer and T. DebRoy: *J. Appl. Phys.*, **93** (2003), 3022.
19) X. He, J. W. Elmer and T. DebRoy: *J. Appl. Phys.*, **97** (2005), 084909.
20) S. Gurevich, M. Amoorezaei, D. Montiel and N. Provatas: *Acta Mater.*, **60** (2012), 3287.
21) M. Tong, J. Liu, Y. Xie, H. B. Dong, R. L. Davidchack, J. Dantzig, D. Ceresoli, N. Marzari, A. Cocks, C. Zhao, I. Richardson, A. Kidess, C. Kleijn, L. Hoglund, S. W. Wen, R. Barnett and D. J. Browne: *IOP Conf. Ser.: Mater. Sci. Eng.*, **33** (2012), 012029.
22) S. A. David and T. DebRoy: *Science*, **257** (1992), 497.
23) M. Schwarz, A. Karma, K. Eckler and D. M. Herlach: *Phys. Rev. Lett.*, **73** (1994), 1380.
24) R. Mathiesen, L. Arnberg, P. Bleuet and A. Somogyi: *Metall. Mater. Trans. A*, **37** (2006), 2515.
25) S. Liu, S.-Z. Lu and A. Hellawell: *J. Cryst. Growth*, **234** (2002), 740.
26) W. J. Boettinger, J. A. Warren, C. Beckermann and A. Karma: *Annu. Rev. Mater. Res.*, **32** (2002), 163.
27) T. Haxhimali, A. Karma, F. Gonzales and M. Rappaz: *Nat. Mater.*, **5** (2006), 660.
28) J. Friedli, P. D. Napoli, M. Rappaz and J. A. Dantzig: *IOP Conf. Ser.: Mater. Sci. Eng.*, **33** (2012), 012111.
29) M. Amoorezaei, S. Gurevich and N. Provatas: *Acta Mater.*, **60** (2012), 657.
30) J.-H. Jeong, N. Goldenfeld and J. A. Dantzig: *Phys. Rev. E*, **64** (2001), 041602.
31) B. P. Athreya, J. A. Dantzig, S. Liu and R. Trivedi: *Philos. Mag.*, **86** (2006), 3739.
32) Y. Xie, H. B. Dong and J. A. Dantzig: *Comput. Mater. Sci.*, **70** (2013), 71.
33) M. Ohno and K. Matsuura: *Phys. Rev. E*, **79** (2009), 031603.
34) M. Ohno and K. Matsuura: *Acta Mater.*, **58** (2010), 5749.
35) Y.-M. Won and B. G. Thomas: *Metall. Mater. Trans. A*, **32** (2001), 1755.
36) B. Echebarria, R. Folch, A. Karma and M. Plapp: *Phys. Rev. E*, **70** (2004), 061604.
37) W. R. Fehlner, S. B. Nickerson and S. H. Vosko: *Solid State Commun.*, **19** (1976), 83.
38) R. Pieters and J. S. Langer: *Phys. Rev. Lett.*, **56** (1986), 1948.
39) E. Brener and D. Temkin: *Phys. Rev. E*, **51** (1995), 351.
40) B. Echebarria, A. Karma and S. Gurevich: Phys. Rev. E, **81** (2010), 021608.
41) M. E. Glicksman: *Metall. Mater. Trans. B*, **43** (2012), 207.
42) M. Ode, J. S. Lee, S. G. Kim, W. T. Kim and T. Suzuki: *ISIJ Int.*, **40** (2000), 870.
43) J. Liu and H. B. Dong: *Comput. Mater. Sci.*, **74** (2013), 92.
44) M. Tong, G. Duggan, J. Liu, Y. Xie, M. Dodge, L. Aucott, H. Dong, R. L. Davidchack, J. Dantzig, O. Barrera, A. Cocks, H. Kitaguchi, S. Lozano-Perez, C. Zhao, I. Richardson, A. Kidess, C. R. Kleijn, S. Wen, R. Barnett and D. J. Browne: *JOM*, **65** (2013), 99.
45) Y.-M. Won and B. G. Thomas: *Metall. Mater. Trans.*, **32** (2001), 1755.
46) W. Kurz, B. Giovanola and R. Trivedi: *Acta Metall.*, **34** (1986), 823.
47) Z. Guo, J. Mi, S. Xiong and P. S. Grant: *Metall. Mater. Trans. B*, **44** (2013), 924